Pushing the grain size limit of pressureless-sintered alumina nanocrystalline ceramics by non-oxidizing atmospheres

Yupeng Wang [a], Hongbing Yang [a,b], Zhengjun Pei [a], Bing Shen [a], Jun Shao [a], Masood Mukhtar [a], Zhikun Ma [a], Herbert Gleiter [a,c], Yanhao Dong [b,*], Tengfei Ma [d,*], Jiangong Li [a,*]

[a] Institute of Materials Science and Engineering, School of Materials and Energy, Lanzhou University, Lanzhou 730000, PR China
[b] State Key Laboratory of New Ceramics and Fine Processing, School of Materials Science and Engineering, Tsinghua University, Beijing 100084, PR China
[c] Institute of Nanotechnology, Karlsruhe Institute of Technology, Karlsruhe 76021, Germany
[d] Key Laboratory of Air-driven Equipment Technology of Zhejiang Province, Quzhou University, Quzhou 324000, PR China

Keywords:
Alumina (α-Al_2O_3)
Nanoparticles
Sintering
Atmosphere
Nanocrystalline ceramics

A B S T R A C T

Nanocrystalline ceramics are of interest due to their refined grains and expected ductility, yet their pressureless sintering is challenging considering the large coarsening driving force and the coupled densification-coarsening kinetics. Of special interest is the pressureless sintering of alumina nanocrystalline ceramics, with fundamental significance to ceramic processing science and technology. Previously reported efforts offered dense alumina nanocrystalline ceramics with average grain size G_{avg} down to 34 nm and with a coarsening ratio β (defined as the ratio of average grain size after and before sintering) of 7.2 from nanoparticles to dense alumina ceramics, by synergistically optimized α-Al_2O_3 nanoparticles and pressureless two-step sintering in air. Here we further pushed G_{avg} down to 29 nm and β down to 5.8, by changing air to non-oxidizing atmosphere (e.g., N_2, Ar, and vacuum). We identified pronounced difference in sintering kinetics in air versus in N_2, Ar, or vacuum, which is unexpected for wide-bandgap, redox-insensitive oxide materials of alumina. With smaller initial nanoparticles (e.g., <3.5 nm) and better optimized sintering conditions, it may be possible to pressureless-sinter dense alumina ceramics with G_{avg} below 20 nm.

1. Introduction

Ceramics are brittle. Refining the grain size of dense polycrystalline ceramics to a few to tens of nanometers may enable grain boundary-mediated plasticity (e.g., grain boundary sliding and grain rotation) before the fracture event. In early explorations, Gleiter *et al.* showed that CaF_2 and TiO_2 nanocrystalline ceramics with an average grain size G_{avg} of ~8 nm could be plastically deformed at 80 and 180 ℃, respectively [1]. Therefore, nanostructuring could provide a plausible pathway towards tough ceramics. Regarding the ceramic materials, Al_2O_3 is among the most important and most useful ceramics. Al_2O_3 ceramics have high hardness, high strength, high temperature resistance, high thermal shock resistance, high wear resistance, electrical insulation, and low cost [2-5]. However, their too low fracture toughness and reliability narrow their usefulness [6,7]. Therefore, many efforts have been made to sinter Al_2O_3 nanocrystalline ceramics [8].

Fabricating dense Al_2O_3 nanocrystalline ceramics via pressureless sintering remains challenging, primarily due to the unavailability of disperse ultrafine α-Al_2O_3 nanoparticles and the rapid growth of grains accompanying the densification process, especially in the final sintering stage [8,9]. When the specific surface area is higher than 100 m^2/g, or the particle size is less than 15 nm, α-Al_2O_3 becomes thermodynamically unstable [10]. Thus it is difficult to synthesize α-Al_2O_3 nanoparticles with sizes <15 nm. Recently, disperse ultrafine α-Al_2O_3 nanoparticles with average particle sizes <10 nm have been successfully prepared in our laboratory [11,12], which makes it possible to sinter Al_2O_3 nanocrystalline ceramics with ultrafine grains under pressureless condition. Furthermore, the two-step sintering proposed by Chen *et al.* has proven to be an effective way for the preparation of nanocrystalline ceramics under pressureless condition owing to its ability to suppress the rapid grain growth in the final sintering stage [13,14]. Typically, from completely dispersed α-Al_2O_3 nanoparticles with an average particle size of 4.7 nm as raw materials and through two-step sintering, Yang *et al.* prepared dense Al_2O_3 nanocrystalline ceramics with an average grain size of 34 nm in our laboratory [15], which represents the grain size limit of Al_2O_3 nanocrystalline ceramics pressureless-sintered so far. The

* Corresponding authors.
E-mail addresses: dongyanhao@tsinghua.edu.cn (Y. Dong), 36105@qzc.edu.cn (T. Ma), lijg@lzu.edu.cn (J. Li).

tricky problem is that the two-step sintering requires the first-step sintering at a higher temperature T_1 to reach a critical relative density (ρ_c, ~83 % for Al_2O_3), so grain growth during the first-step sintering is unavoidable, which also determines the final grain size of the sintered ceramics to a certain extent. If one could accelerate the densification to achieve ρ_c at a lower T_1, it would be possible to prepare dense Al_2O_3 nanocrystalline ceramics of finer grains by two-step sintering under pressureless condition.

In general, mass transfer during pressureless sintering of solid-phase systems is accomplished through three main pathways, i.e., surface diffusion, lattice diffusion, and grain boundary diffusion. Although surface diffusion-induced particle rearrangement increases the density of the samples in the initial sintering stage [16,17], surface diffusion is considered to be a non-dominant densification mechanism because it does not directly lead to an increase in the density of the samples in the intermediate and final sintering stage [18]. Lattice diffusion and grain boundary diffusion are the primary mechanisms responsible for densification in the intermediate and final sintering stage; and the latter is regarded as being dominant at relatively lower temperatures due to its smaller activation energy compared to lattice diffusion [19-23]. Considering the high sintering activity of nanoparticles (at typical sintering temperatures <1300 ℃) and the large volume fraction of grain boundaries in nanocrystalline samples, it is widely accepted that the main densification mechanism of α-Al_2O_3 nanoparticle green bodies during pressureless sintering is grain boundary diffusion [6,8]. Coble reported that the dependence of sintering rate of oxides on sintering atmosphere was attributed to a change in vacancy concentration with changing oxygen partial pressure (P_{O2}). Additionally, the diffusion coefficient would be increased by increasing the vacancies of the slower diffusing species, which increases the sintering rate of sintered samples [24]. For Al_2O_3 ceramics, the grain boundary diffusion is mainly dominated by slower oxygen atom diffusion [25]. Therefore, it is feasible to promote densification of α-Al_2O_3 nanoparticles by introducing extra oxygen vacancies via changing P_{O2}, which can accelerate oxygen atom diffusion and densify ultrafine-grained Al_2O_3 nanocrystalline ceramics.

Atmospheres with low oxygen partial pressure P_{O2} can induce more oxygen vacancies in oxide polycrystals. So sintering in low P_{O2} atmospheres such as Ar, N_2, and H_2 atmospheres and vacuum have been reported to assist sintering in oxide material systems [26-29]. For example, Walker reported the effect of sintering atmosphere on sintering rate of Al_2O_3 ceramics and found that a higher density can be obtained in low P_{O2} atmospheres (such as H_2 and Ar) compared to air under the same sintering condition [27]. Kitazawa and Coble reported that the ionic transference number decreases from 0.21 to 0.01 as P_{O2} increases from 10^{-15} to 10^{-9} atm in MgO-doped Al_2O_3 ceramics [28]. Recently, Han *et al.* systematically investigated the effect of pre-sintering atmosphere (air and vacuum) on the densification process, microstructure evolution, and final optical quality of $MgO{\bullet}nAl_2O_3$ (n = 1.1 and 1.5) ceramics; they observed that the samples sintered in vacuum show higher density compared to those sintered in air under the same sintering conditions [29]. However, as far as we know, the sintering behaviors of α-Al_2O_3 nanoparticles in various sintering atmospheres have not been explored so far, due to difficulties in preparation of disperse ultrafine α-Al_2O_3 nanoparticles. This missing gap has motivated our current study, and here we report for the first time the preparation of dense fine-grained Al_2O_3 nanocrystalline ceramics by pressureless sintering in low P_{O2} atmospheres.

In the present work, we first investigated the sintering behaviors and kinetics of home-made high-purity, well dispersed, and ultrafine α-Al_2O_3 nanoparticles of 7.4 nm average particle size in various atmospheres including air, vacuum, N_2, and Ar. The results show that the densification of α-Al_2O_3 nanoparticles was significantly promoted by low P_{O2} atmospheres without causing discernible grain growth. Further kinetic analyses revealed that sintered samples of α-Al_2O_3 nanoparticles have lower activation energy of grain boundary diffusion when sintered in low P_{O2} atmospheres compared to air, and the possible reasons for this will be discussed. Then, in combination with a two-step sintering, a series of dense and fine-grained Al_2O_3 nanocrystalline ceramics were successfully obtained in various atmospheres. In particular, the average grain size of the Al_2O_3 nanocrystalline ceramics two-step sintered in N_2 from 5.0 nm α-Al_2O_3 nanoparticles is 29 nm, which represents the smallest grain size of dense Al_2O_3 nanocrystalline ceramics achieved so far by pressureless sintering.

2. Experimental procedures

In the present work, ultrafine α-Al_2O_3 nanoparticles were prepared using ball milling followed by a corrosion-fractionated coagulation separation process, similar to the one employed in our previous works [11,12]. The micron-sized high-purity α-Al_2O_3 particles were milled 20 h at 250 rpm using a ball to powder ratio of 10: 1 on a Fritsch P4 planetary ball mill (Fritsch, Germany). The as-milled powders were corroded using 12 mol/L hydrochloric acid (HCl) to remove the impurities (such as Fe and Cr) introduced through stainless steel milling jars and balls. Fractionated coagulation method was employed to separate disperse α-Al_2O_3 nanoparticles with different average particle sizes. Only by changing the concentration of coagulation agent, α-Al_2O_3 nanoparticles with different average particle sizes can be obtained since nanoparticles of different particle sizes have different critical concentrations of coagulation. In our present work, HCl solutions with different HCl concentrations were used as coagulation agent to achieve size-selective separations by refined fractionated coagulation. Typically, the corroded α-Al_2O_3 particles were separated using 1.8 and 1.0 mol/L HCl to obtain 5.0 and 7.4 nm α-Al_2O_3 nanoparticles, respectively. Finally, both the separated nanoparticles were collected using 12 mol/L HCl and dried at 60 ℃ for 24 h. The uniaxial pressing of the α-Al_2O_3 nanoparticles at 750 MPa for 2 h at room temperature resulted in green bodies with a diameter of 6 mm, a thickness of 0.5 mm, and a relative density of 60 %. The green bodies of 7.4 nm α-Al_2O_3 nanoparticles were used to study their sintering behaviors and kinetics in various atmospheres. Four kinds of atmospheres including air, vacuum, N_2, and Ar were employed in pressureless sintering. The vacuum sintering was performed in vacuum of ~5×10^4 Pa (P_{O2}≈1×10^4 Pa) and ~50 Pa (P_{O2}≈10.5 Pa). The high-purity N_2 and Ar (>99.999 %, P_{O2}≈0.02 Pa) of ambient atmospheric pressure were used in N_2 and Ar sinterings. Finally, 5.0 nm α-Al_2O_3 nanoparticles were used to prepare dense Al_2O_3 nanocrystalline ceramic in N_2.

In this study, two types of pressureless sintering schedules were conducted in different atmospheres: (i) Constant-heating-rate sintering without holding: the green bodies were heated to predetermined temperatures ranging from 700 to 1200 °C at 10 °C/min without holding, followed by immediately cooling down to room temperature at 5 °C/min. This schedule was utilized to study the sintering behaviors and kinetics and to explore the appropriate first-step sintering temperature for subsequent two-step sintering. (ii) Two-step sintering: the green bodies were firstly heated at 10 °C/min to a higher first-step sintering temperature T_1 without holding, then immediately cooled down to a lower second-step sintering temperature T_2 at 5 °C/min, held for certain durations at T_2, and finally cooled down to room temperature at 5 °C/min. This sintering trajectory was utilized for the preparation of dense fine-grained Al_2O_3 nanocrystalline ceramics. The densities of both the green bodies and sintered samples were measured using the geometry method for relative densities ρ<80 % theoretical density or Archimedes' method for ρ>80 %. A density value of 3.96 g/cm^3 for α-Al_2O_3 was used to calculate the relative density ρ (in consistency with our previous works [6,15,30,31]). Densification rates $d\rho/dt$ in constant-heating-rate experiments were determined based on the average slopes between each sintering data point and its two neighboring data points in the ρ-t plot.

The phase of the α-Al_2O_3 nanoparticles was analyzed by X-ray diffraction (XRD) on a D/max-2400 diffractometer (Rigaku, Japan)

using Cu K_α radiation. The morphologies of α-Al_2O_3 nanoparticles and sintered samples (with grain sizes <20 nm) were characterized by transmission electron microscopy (TEM) on an FEI Tecnai G2 F30 electron microscope (FEI, USA) operated at an accelerating voltage of 300 kV. The inductively coupled plasma-atomic emission spectrometry (ICP-AES) was applied to analyze the compositions of α-Al_2O_3 nanoparticles on an IRIS Advantage spectrometer (Thermo Jarrell Ash, USA). The fracture surfaces of sintered samples (with grain sizes >20 nm) were characterized by scanning electron microscopy (SEM) on a Hitachi SU8010 electron microscope (Hitachi, Japan) operated at 15 kV. Particle/grain size distributions and average particle/grain sizes were statistically determined from over 500 particles/grains observed by TEM and/or SEM in difference areas of the samples. Vickers microhardness tests were conducted on the almost dense Al_2O_3 nanocrystalline ceramics sintered in N_2 after polishing, under 500 g (4.91 N) load with 10 s duration on a HYHVS-1000T Vickers Microhardness Tester (Wuyi Hengyu, China). Typically, the average microhardness values were determined by measuring over 5 tests and the distance between the two indentations was set larger than 500 μm. After testing, the lengths of the diagonals of the indentations on the surface were observed by SEM and the microhardness H_V was calculated using [32]

$$H_V = 1854.4\frac{P}{d^2} \quad (1)$$

where H_V is the microhardness in GPa, P presents the applied load in N, and d is the average of the diagonal lengths of indentations in μm. Fracture toughness K_{Ic} was also evaluated based on the indentation morphology using the following equation [33],

$$K_{Ic} = 0.016\left(\frac{E}{H_V}\right)^{0.5}\frac{P}{c^{1.5}} \quad (2)$$

where E is the elastic modulus of the material (380 GPa for Al_2O_3 [34]), and c presents the half-length of the cracks of indentations (μm).

3. Results

3.1. Synthesized nanoparticles

The α-Al_2O_3 nanoparticles separated at 1.0 mol/L HCl were characterized using XRD and TEM, and the results are presented in Fig. 1. The XRD pattern in Fig. 1a matches well the pattern of α-Al_2O_3 (JCPDS No. 75–1862) [35], indicating that the nanoparticles are pure α-Al_2O_3 phase. The broadening of the diffraction peaks implies that the α-Al_2O_3 nanoparticles have fine grains [15]. The TEM image in Fig. 1b demonstrates that the nanoparticles are dispersed, ultrafine in size, and equiaxial in shape. The particle size distribution in Fig. 1c reveals that the α-Al_2O_3 nanoparticles have a narrow size distribution of 3–12 nm, a small standard deviation σ (0.23) of the normalized particle/grain size distribution, and an average particle size of 7.4 nm. The ICP-AES results in Table 1 reveals that the Fe and Cr impurities are only 0.049 and 0.008 wt % of the total mass, respectively. These results correspond to a purity of 99.943 % Al_2O_3 (mass percent) of the ultrafine α-Al_2O_3 nanoparticles.

3.2. Constant-heating-rate sintering without holding

It is worth noting that the corrosion methodology used to prepare fine nanoparticles will introduce nonequilibrium defects at the surface of the nanoparticles. These defects could influence the sintering and densification behaviors of ceramics. In particular, the presence of massive nonequilibrium defects may alter the surface energy and reactivity of the nanoparticles, affecting their sintering behavior during densification. To compare the sintering behaviors of 7.4 nm α-Al_2O_3 nanoparticles in air and low P_{O2} atmospheres (vacuum (~50 Pa), N_2, and Ar), the constant-heating-rate sintering experiments without holding were performed. The typical SEM images of partially and/or fully sintered Al_2O_3 ceramics are shown in Fig. 2, and the σ of the sintered samples are also inserted. The obtained relative density ρ, densification rate $d\rho/dt$, and average grain size G_{avg} results of all the sintered samples as a function of sintering temperature are plotted in Fig. 3. It can be found from Fig. 2 that a uniform microstructure with equiaxial grains appear in all samples, indicating no abnormal grain growth at $T \leq 1200$ °C in all atmospheres. When sintered at 1000 °C, the samples all have significant porosity and a similar average grain size of about 34 nm, which is not strongly dependent on the sintering atmospheres (Fig. 2a–d). As the sintering temperature increases from 1000 to 1100 °C, the samples sintered in different atmospheres show different volumes of pores but still have similar average grain size of about 52 nm (Fig. 2e–h). The sample sintered in air has a large number of pores (Fig. 2e). In contrast, the samples sintered in N_2 and Ar contain only a few pores (Fig. 2 g and h). After sintering at 1200 °C, there are no visible pores present in any samples (indicating nearly full density achieved). All sintered Al_2O_3 samples still have a similar average grain size of about

Table 1
ICP-AES results of 7.4 nm α-Al_2O_3 nanoparticles.

Element	Concentration (mg/L)	Mass% of cations	Mass% of total	Cations %
Al	401.29	99.893	52.893	99.947
Fe	0.37	0.093	0.049	0.045
Cr	0.06	0.014	0.008	0.008

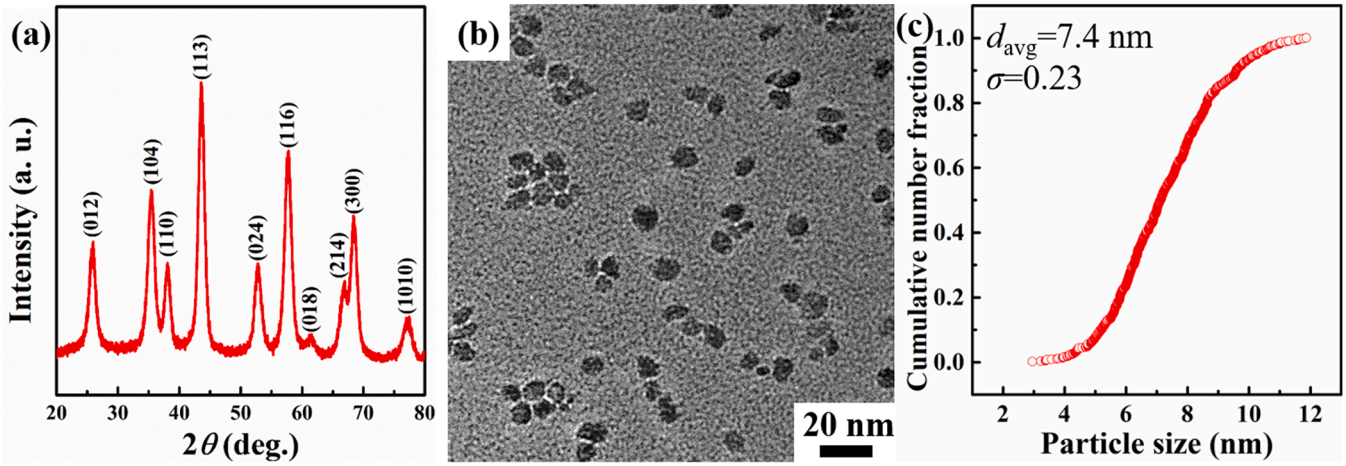

Fig. 1. XRD pattern (a), TEM image (b), and particle size distribution (c) of the α-Al_2O_3 nanoparticles separated at 1.0 mol/L HCl.

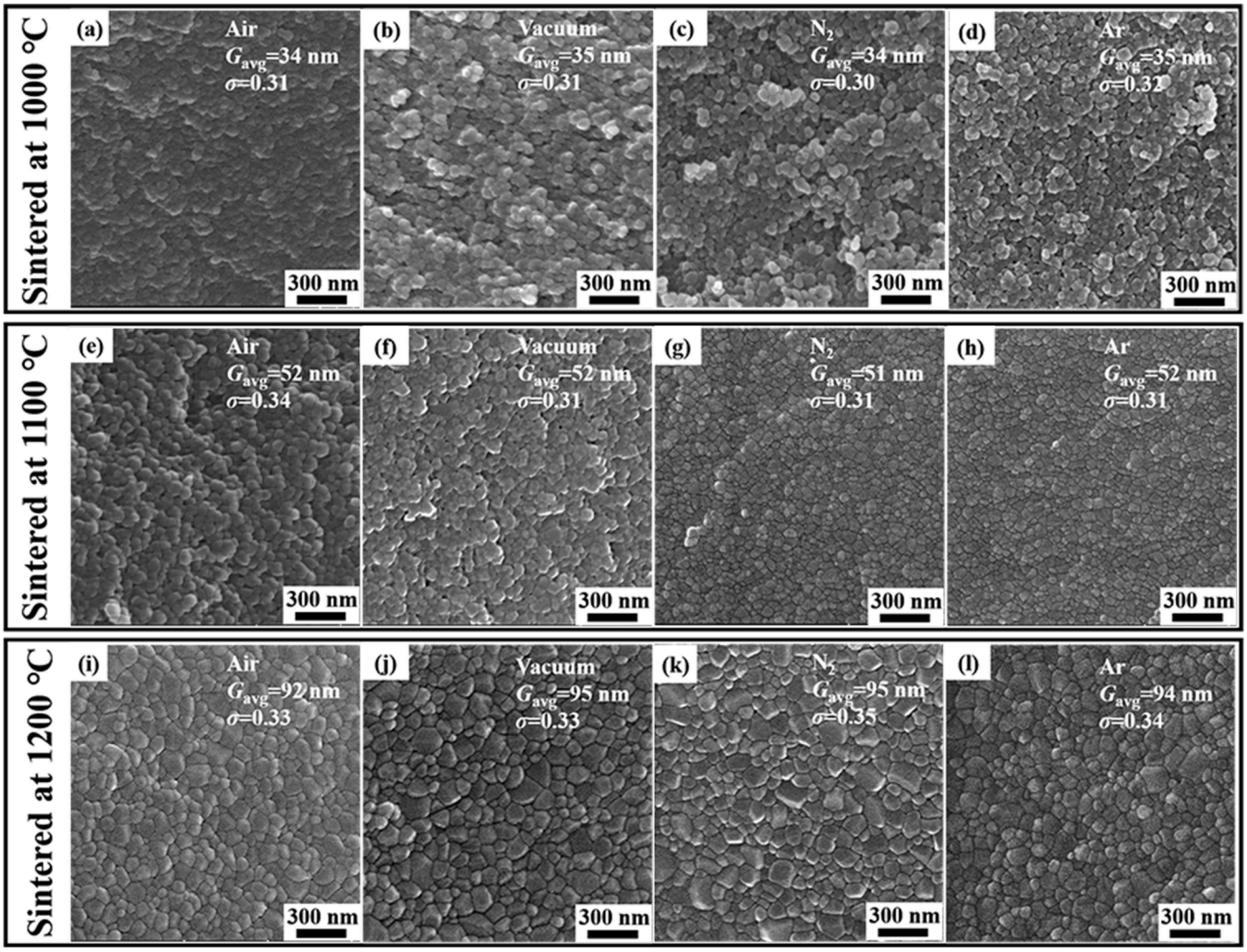

Fig. 2. SEM images of 7.4 nm green bodies sintered at 1000, 1100, and 1200 °C without holding in air (a, e, and i), vacuum (b, f, and j), N_2 (c, g, and k), and Ar (d, h, and l).

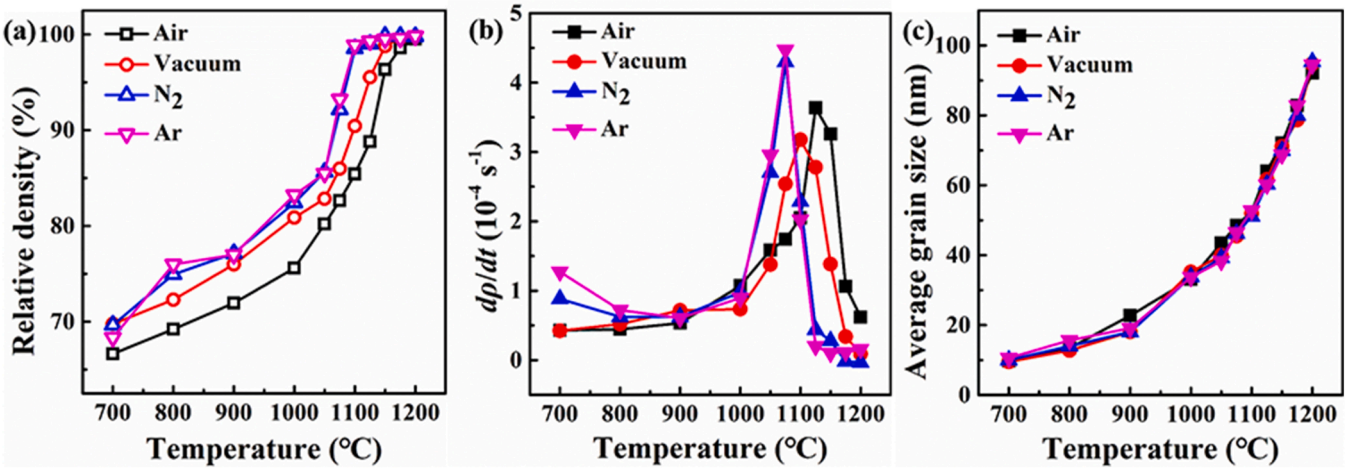

Fig. 3. Sintering curves of the green bodies of the 7.4 nm α-Al_2O_3 nanoparticles in constant-heating-rate sintering experiments without holding in different atmospheres: relative density (a), densification rate $d\rho/dt$ (b), and average grain size (c) as a function of sintering temperature.

95 nm (Fig. 2i–l).

Fig. 3 illustrates the sintering curves of the green bodies of the 7.4 nm α-Al_2O_3 nanoparticles in the constant-heating-rate sintering experiments. We found that the densification of the green bodies is substantially influenced by the sintering atmospheres. At the same sintering temperature, the relative densities of the samples sintered in air

are notably lower than those sintered in vacuum, N_2, and Ar. The sintering temperature at which the sample reaches nearly complete densification (ρ=99.1 %) is 1200 °C in air whereas the temperatures for nearly complete densification in vacuum (ρ=98.8 %), N_2 (ρ=98.5 %), and Ar (ρ=98.9 %) are 1150, 1100, and 1100 °C, respectively (Fig. 3a). It should be noted that the temperatures for nearly complete densification of the 7.4 nm α-Al_2O_3 nanoparticles are much lower than that of micron or submicron-sized α-Al_2O_3 particles (>1400 °C). This indicates that our 7.4 nm α-Al_2O_3 nanoparticles exhibit superior sinterability. The above results manifest that vacuum, N_2, and Ar with low P_{O2} promote the densification of α-Al_2O_3 nanoparticles. This can also be seen from the variation curves of the densification rate $d\rho/dt$ with sintering temperature in Fig. 3b. The fastest densification occurs at ~1125 °C for sintering in air (~3.6 × 10^{-4} s^{-1}) while the fastest densification appears at ~1100, ~1075, and ~1075 °C for sintering in vacuum (~3.2 × 10^{-4} s^{-1}), N_2 (~4.3 × 10^{-4} s^{-1}), and Ar (~4.4 × 10^{-4} s^{-1}), respectively. Interestingly, though the α-Al_2O_3 nanoparticles exhibit different densification behaviors in different atmospheres (Fig. 3a and b), all the samples sintered at the same temperature but in different atmospheres have similar average grain sizes, as shown by the G_{avg} versus sintering temperature curves in Fig. 3c. This implies that unlike the densification behavior, the grain growth of the green bodies of the α-Al_2O_3 nanoparticles may not be strongly dependent on sintering atmospheres.

The sintering trajectories (G_{avg}-ρ plots) of the 7.4 nm α-Al_2O_3 nanoparticles in various sintering atmospheres are plotted in Fig. 4. Obviously, all G_{avg}-ρ trajectories exhibit a similar path. G_{avg} increases almost linearly with ρ in the ρ<~96 % range, followed by a rapid grain growth in the ρ>~96 % range. This is consistent with the phenomenon observed in the sintering experiments of the 4.7 nm α-Al_2O_3 nanoparticles in our previous work [15]. The similarity of the sintering trajectories suggests that the low P_{O2} atmospheres do not change the densification mechanism of α-Al_2O_3 nanoparticles, namely, the dominant densification mechanism of α-Al_2O_3 nanoparticles remains grain boundary diffusion when sintered in air, vacuum, N_2, and Ar.

3.3. Sintering kinetics from constant-heating-rate experiments

It is reasonable to assume that the grain boundary diffusion is the main densification mechanism for sintering our ultrafine α-Al_2O_3 nanoparticles based on the sintering results (fine grains <100 nm obtained at low temperature ≤1200 °C). The sintering kinetics of the α-Al_2O_3 nanoparticles in different atmospheres were investigated by means of two well-established classical models combined with the constant-heating-rate sintering data in Section 3.2. The first model is that proposed by Johnson and later on adapted by Young and Cutler [36] using the following sintering equation,

$$\left(\frac{\Delta L}{L_0}\right)^{2.06}\frac{d(\Delta L/L_0)}{dt}=\frac{11.2\gamma\Omega\delta D_{GB}}{k_B T G_{avg}^4} \quad (3)$$

where $\Delta L/L_0$ is the linear shrinkage (L_0 and ΔL are the initial thickness and change in thickness of green bodies during sintering, respectively, which were measured five times using micrometer (0.001 mm in precision, Sanliang, Japan) on each sample and took an average), t is the time, γ is the grain boundary energy (1.97 J/m^2 for Al_2O_3) [37], Ω is the atomic volume (4.28 × 10^{-29} m^3 for Al_2O_3), δ is the grain boundary thickness (1 nm, as observed in our previous study [15]), D_{GB} is the grain boundary diffusion coefficient, k_B is the Boltzmann constant, T is the absolute temperature, and G_{avg} is the average grain size. The sintering data above 1000 °C in air, above 900 °C in vacuum, and above 800 °C in N_2 and in Ar with 75 %<ρ<90 % (where major sintering event takes place) were analyzed using Johnson's model. The calculated D_{GB} and the fitted grain boundary diffusion activation energy E_a (via the Arrhenius equation, i.e., $D_{GB}=D_{GB,0}\exp(-E_a/RT)$) are plotted in Fig. 5a and listed in Table 2, respectively. For the sintering in air, the fitted E_a is 5.10 eV. For the vacuum sintering, E_a is 4.32 eV. For the N_2 sintering, E_a is 3.31 eV. And for the Ar sintering, E_a is 3.06 eV.

We then analyzed the sintering kinetics by the sintering model proposed by Herring [38],

$$\frac{d\rho}{\rho dt}=F(\rho)\frac{3\gamma\Omega\delta D_{GB}}{k_B T G_{avg}^4} \quad (4)$$

where $F(\rho)$≈12,000 for 75 %<ρ<85 % under Hansen's assumption [39]. The calculated D_{GB} and the fitted E_a are plotted in Fig. 5b and listed in Table 2, respectively. For the air sintering, the fitted E_a is 3.73 eV. E_a for the vacuum sintering is 3.52 eV. E_a for the N_2 sintering is 2.51 eV. And E_a for the Ar sintering is 2.58 eV. Although there exists some dissimilarity in the E_a values obtained by the Johnson's and Herring's models (the E_a obtained through the Johnson's are larger than those from the Herring's model, which is consistent with the phenomenon reported in literature [30,31,40,41]), it can be found from Table 2 that (1) the E_a values (5.10 eV for Johnson's model and 3.73 eV for Herring's model) obtained from the air sintering data are similar to the air sintering results reported in literature (in the range of 5.14–6.16 eV for Johnson's model and 3.54–4.58 eV for Herring's model for α-Al_2O_3 sintered in air). (2) The E_a values of the samples sintered in vacuum (4.32 eV for Johnson's model and 3.52 eV for Herring's model), N_2 (3.31 eV for Johnson's model and 2.51 eV for Herring's model), and Ar (3.06 eV for Johnson's model and 2.58 eV for Herring's model) are obviously smaller than those sintered in air, which is consistent with the low sintering temperature required to reach full density and implies high sinterability in vacuum, N_2, and Ar atmospheres.

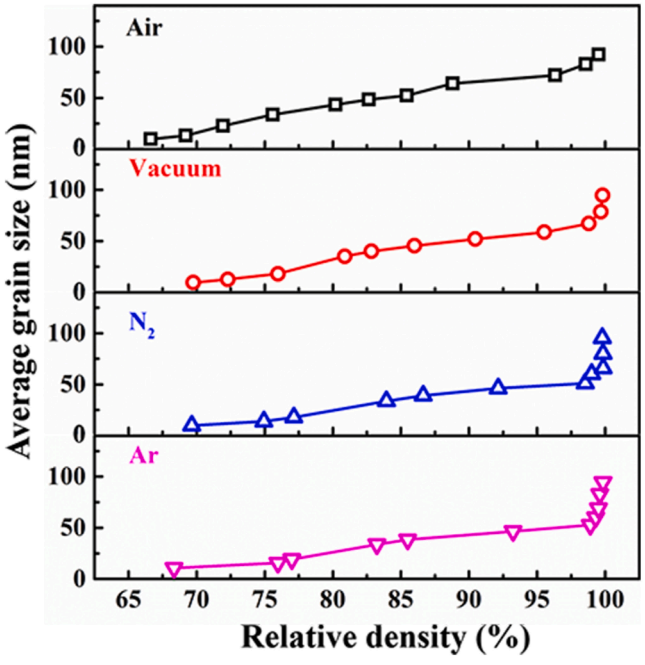

Fig. 4. Average grain size-relative density sintering trajectories of the Al_2O_3 samples sintered in air, vacuum, N_2, and Ar.

3.4. Two-step sintering

Fully dense Al_2O_3 nanocrystalline samples with an average grain size of G_{avg}=51 nm can be prepared in N_2 via constant-heating-rate sintering without holding at 1100 °C (Fig. 2g), from the α-Al_2O_3 nanoparticles with an average particle size of 7.4 nm. To inhibit rapid grain growth in the final sintering stage and obtain fully dense Al_2O_3 nanocrystalline ceramics with average grain sizes G_{avg}<50 nm, two-step sintering was utilized and optimized. In two-step sintering, the green bodies were firstly heated to a higher first-step sintering temperature T_1 without

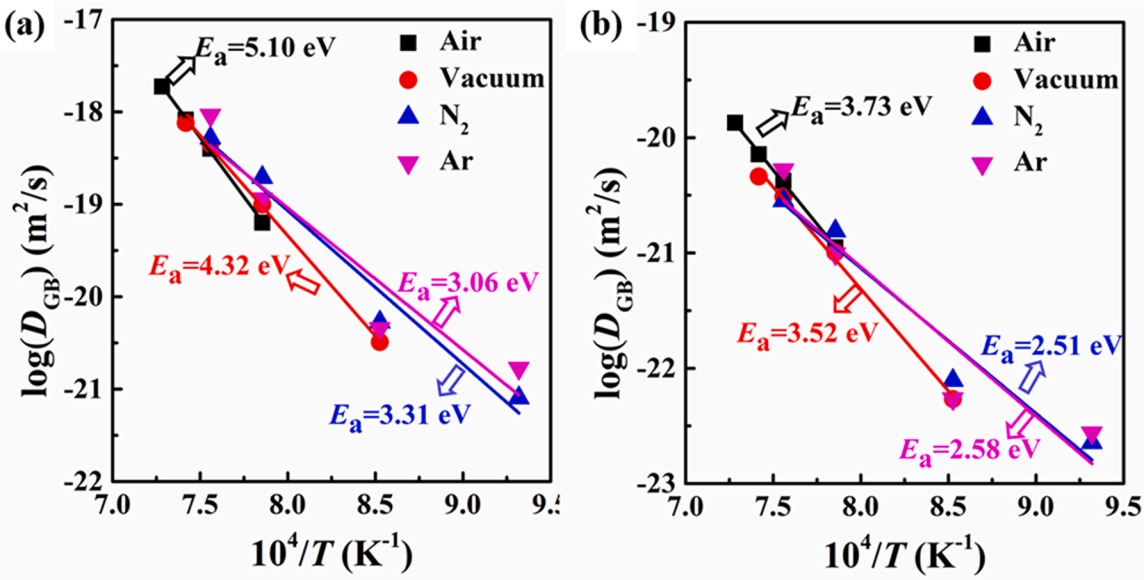

Fig. 5. Arrhenius plots of grain boundary diffusivity values in different atmospheres calculated by Johnson's model (a) and Herring's model (b).

Table 2
Calculated activation energies for grain boundary diffusion in Al_2O_3 ceramics using pressureless sintering data in different atmospheres in our present work and reported in literatures.

Average particle size	Activation energy E_a (eV)		Atmosphere (Reference)
	Johnson's model	Herring's model	
7.4 nm	5.10	3.73	Air
7.4 nm	4.32	3.52	Vacuum
7.4 nm	3.31	2.51	N_2
7.4 nm	3.06	2.58	Ar
4.5 nm	5.14	3.99	Air [30]
4.7 nm	5.22	3.75	Air [31]
9.0 nm	5.09	3.54	Air [40]
16 nm	6.16	4.58	Air [41]
62 nm	5.40	3.87	Air [41]

holding to achieve the critical relative density ρ_c (at ρ_c the pores are in a thermodynamically unstable state; ρ_c=~83 % for Al_2O_3 [6,15,31]) and then cooled to a lower second-step sintering temperature T_2, and held at T_2 for some duration to reach full density without significant grain growth.

According to the above constant-rate-sintering results (Figs. 3 and 4), the sample with a relative density of ρ=85.4 % and an average grain size of G_{avg}=52 nm sintered at 1100 ℃ without holding in air, the sample with ρ=85.6 % and G_{avg}=39 nm sintered at 1050 ℃ without holding in N_2, and the sample with ρ=85.4 % and G_{avg}=38 nm sintered at 1050 ℃ without holding in Ar have relative densities ρ larger than the critical relative density ρ_c (~83 %). So 1100, 1050, and 1050 ℃ are selected as T_1 for two-step sintering of the green bodies of the 7.4 nm α-Al_2O_3 nanoparticles in air, N_2, and Ar, respectively. Specifically, we found that (1) the sample sintered at T_1=1100 ℃ without holding and at T_2=1000 ℃ for 20 h (minimal holding times to achieve >99 % relative density) in air (Fig. 6a and b) has ρ=99.1 %, G_{avg}=55 nm, and coarsening ratio β (defined as the ratio of the average grain size after sintering to the average size of the initial powders before sintering)=7.4; (2) the sample sintered at T_1=1050 ℃ without holding and at T_2=950 ℃ for 20 h in N_2 (Fig. 6c and d) possesses ρ=99.2 %, G_{avg}=38 nm, and β=5.1; and (3) the sample sintered at T_1=1050 ℃ without holding and at T_2=950 ℃ for 20 h in Ar (Fig. 6e and f) exhibits ρ=99.4 %, G_{avg}=38 nm, and β=5.1. None of the two-step sintered samples experiences obvious grain growth during the second-step sintering and all have a uniform microstructure.

Compared to the sample two-step sintered in air, the samples two-step sintered in N_2 and Ar require low sintering temperatures to achieve full density and thus have finer grains. The G_{avg} of the samples two-step sintered in N_2 and Ar (38 nm) from the 7.4 nm nanoparticles is even close to that of the sample two-step sintered in air (G_{avg}=34 nm) from the 4.7 nm nanoparticles [15], though the average size of the starting nanoparticles used in our present study is about 1.6 times of that in the latter study.

To be more confident of the effect of oxygen partial pressure P_{O2} on the sintering behavior of Al_2O_3 nanocrystalline ceramics in a wider range of P_{O2}, two-step sinterings were further carried out at the same sintering condition but at different vacuum levels (~1×10^5, ~5×10^4, and ~50 Pa corresponding to P_{O2} values of ~2×10^4, 1×10^4, and 10.5 Pa, respectively). Similarly, it can be found from Figs. 3 and 4 that the sample with ρ=85.6 % and G_{avg}=46 nm sintered at 1075 ℃ without holding in ~50 Pa vacuum exhibits relative density ρ>83 %, so 1075 ℃ was selected as T_1 for two-step sintering of the 7.4 nm α-Al_2O_3 nanoparticle green bodies at different vacuum levels. The typical characteristics of the sintered samples are shown in Fig. 7. Interestingly, the Al_2O_3 samples two-step sintered at T_1=1075 ℃ without holding and T_2=975 ℃ for 20 h at different vacuum levels show different relative densities but similar grain sizes around 46 nm. All sintered samples have uniform microstructure (Fig. 7a, c, and e), unimodal grain size distribution (Fig. 7b, d, and f), and nearly equiaxed grains without abnormal grain growth. Typically, the sample sintered in air (Fig. 7a and b) shows ρ=91.3 %, G_{avg}=46 nm, and β=6.2; the sample sintered in ~5×10^4 Pa vacuum (Fig. 7c and d) exhibits ρ=92.6 %, G_{avg}=48 nm, and β=6.5; the sample sintered in ~50 Pa vacuum (Fig. 7e and f) displays ρ=99.3 %, G_{avg}=46 nm, and β=6.2. These results suggest that the Al_2O_3 nanocrystalline ceramics can be densified completely by decreasing P_{O2} under the same two-step sintering condition. This is mainly attributed to the higher relative density obtained after first step sintering at T_1 without holding at lower P_{O2}, which is beneficial to densification during the second step sintering at T_2.

3.5. Pushing the grain size limit using finer nanoparticles via non-oxidizing atmospheres

To further obtain dense Al_2O_3 nanocrystalline ceramics with average grain sizes G_{avg}<30 nm, 5.0 nm α-Al_2O_3 nanoparticles (Fig. 8a and b) were pressed into green bodies and two-step sintered in N_2. The green bodies of the 5.0 nm nanoparticles reach a relative density of 85.5 %

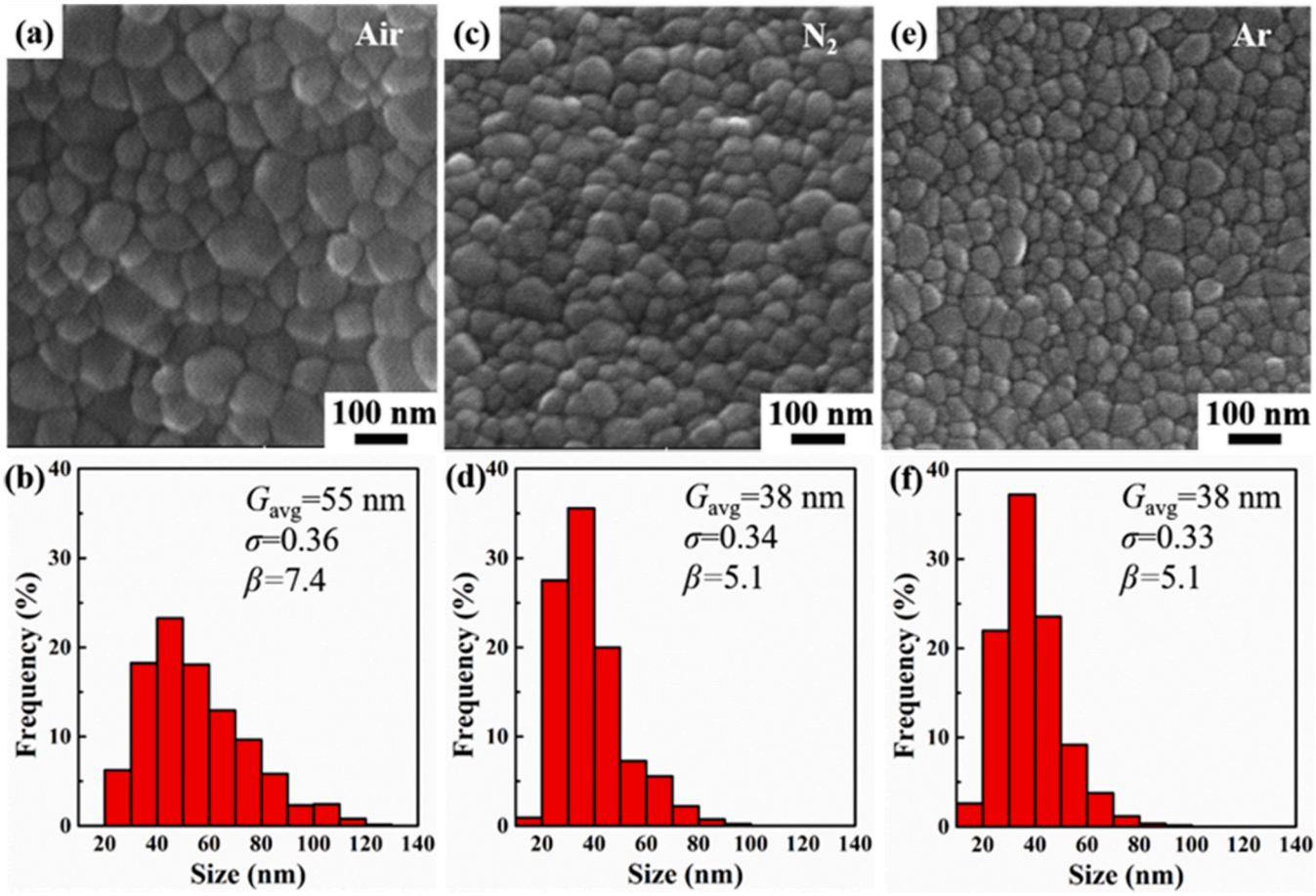

Fig. 6. SEM images (a, c, and e) and grain size distributions (b, d, and f) of Al_2O_3 nanocrystalline ceramics two-step sintered in air at T_1 1100 and T_2 1000 ℃ for 20 h (a, b), in N_2 at T_1 1050 and T_2 950 ℃ for 20 h (c, d), and in Ar at T_1 1050 and T_2 950 ℃ for 20 h (e, f).

(>ρ_c~83 %) with G_{avg}=28 nm (Fig. 8c and d) after the first-step sintering at T_1=1000 ℃ without holding in N_2. When cooled to and held at T_2=900 ℃ for 40 h (minimal holding times to achieve >99 % relative density), the fully dense Al_2O_3 nanocrystalline ceramic was obtained without obvious grain growth. The sintered sample has relative density ρ=99.5 % and an ultra-uniform microstructure (Fig. 8e) which shows fine equiaxed grains between 10 and 75 nm and a unimodal grain size distribution with an average gain size of G_{avg}=29 nm (Fig. 8f). It is worth noting that the average gain size G_{avg}=29 nm of this Al_2O_3 nanocrystalline ceramic is 5.8 times of the initial nanoparticle size (5.0 nm), much lower than 7.2 times of the initial nanoparticle size (4.7 nm) for the Al_2O_3 nanocrystalline ceramic (34 nm) two-step sintered in air [8, 15]. This "advantage" may stem from the increased oxygen vacancy concentration in grain boundaries of Al_2O_3 in low P_{O2} atmospheres which can lower the energy barrier for grain boundary diffusion and increase the grain boundary diffusivity. This demonstrates the effectiveness and feasibility of the low P_{O2} atmosphere two-step sintering for the preparation of fine-grained Al_2O_3 nanocrystalline ceramics. To the best of our knowledge, the average grain size of G_{avg}=29 nm is the smallest average grain size reported to date in dense Al_2O_3 nanocrystalline ceramics achieved by pressureless sintering.

3.6. Microhardness and fracture toughness

To demonstrate the superior mechanical properties of Al_2O_3 nanocrystalline ceramics with different grain sizes, we conducted Vickers indentation tests on the polishing surfaces of pure Al_2O_3 nanocrystalline ceramics with G_{avg}=38 and 95 nm. The H_V and K_{Ic} were evaluated from the indentations observed by SEM, as exhibited in Fig. 9. The SEM observations of the indentations (inserted in Fig. 9a) reveal that similar fracture behaviors occur at various grain sizes. The formation of cracks can be clearly observed around the indentations in the Al_2O_3 nanocrystalline ceramics with different grain sizes. Interestingly, as the average grain size increases from 38 to 95 nm, the diagonal length of indentation decreases obviously, while the crack length increases significantly. This indicates that the Al_2O_3 nanocrystalline ceramic with G_{avg}=38 nm shows a lower H_V but higher K_{Ic} compared to the Al_2O_3 nanocrystalline ceramic with G_{avg}=95 nm. The H_V data are plotted against G_{avg} in Fig. 9a and compared with literature data [42-49], revealing that the Hall-Petch relationship holds until the G_{avg} reduced to ~90 nm (higher H_V = 26.4 GPa can be obtained for the Al_2O_3 nanocrystalline ceramic with G_{avg}=95 nm in this work). The higher H_V indicates that Al_2O_3 nanocrystalline ceramic with G_{avg}=95 nm still has good grain boundary cohesion without softening. However, it is worth noting that a relatively low H_V (18.7 GPa) is obtained for G_{avg}=38 nm. The K_{Ic} data of Al_2O_3 ceramics with different G_{avg} are plotted in Fig. 9b and compared with literature data [43,47,48,50], which presents the sample with a smaller G_{avg} (38 nm) showing a higher K_{Ic} (4.06 MPa•$m^{1/2}$) among all the dense pure Al_2O_3 ceramics.

4. Discussions

From the above results, it can be concluded that the densification of the α-Al_2O_3 nanoparticles is strongly affected by the sintering temperature and atmospheres during pressureless sintering. It is worth noting that the G_{avg} results of the Al_2O_3 samples sintered at the same temperature in different atmospheres are similar (Fig. 2), implying that different sintering atmospheres mainly affect the densification and have

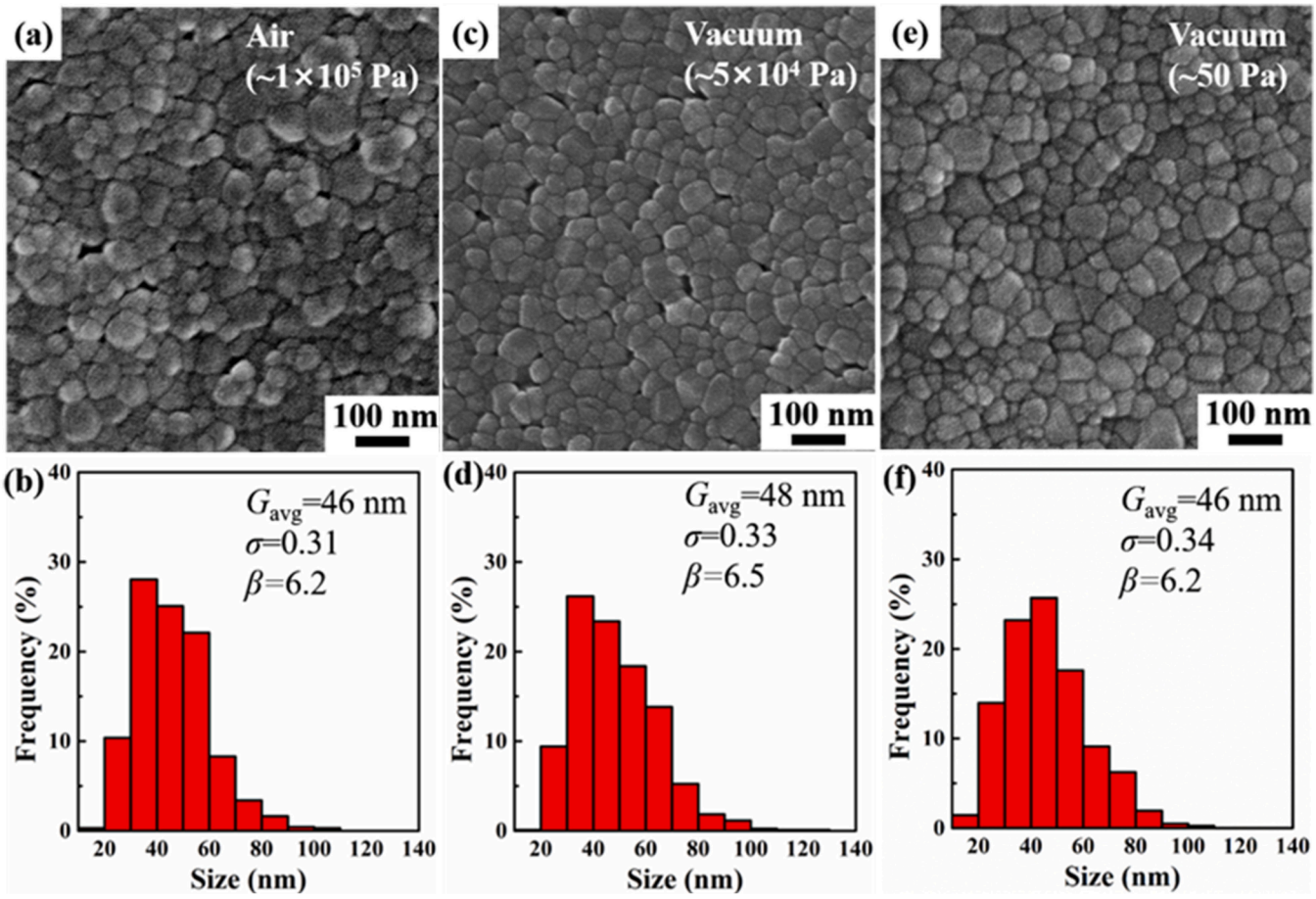

Fig. 7. SEM images (a, c, and e) and grain size distributions (b, d, and f) of Al_2O_3 nanocrystalline ceramics two-step sintered in air (a, b), ~5 × 10^4 Pa vacuum (c, d), and ~50 Pa vacuum (e, f) at T_1 1075 without holding and T_2 975 ℃ for 20 h.

little effect on grain growth. The obtained results from the sintering curves demonstrate that the densification is significantly affected by low P_{O2} atmospheres (Fig. 3a). The vacuum, N_2, and Ar atmospheres exhibit obviously enhanced densification compared to air. However, a similar density can be achieved at lower temperatures in vacuum, N_2, and Ar, at which the sintered samples have smaller grains (Fig. 3a and c). This "positive" effect of the vacuum, N_2, and Ar atmospheres on the sintering of α-Al_2O_3 nanoparticles is beneficial for the preparation of Al_2O_3 nanocrystalline ceramics with ultrafine grains. Typically, the enhancement of densification was well known for oxide material systems sintered in low P_{O2} environments, especially in a reducing atmosphere [27,29,51-53]. And the higher densification rate in lower P_{O2} environments can be due to more oxygen vacancies formed in grain boundaries induced by lower P_{O2} [29].

However, only a few studies reported the grain boundary oxygen vacancies participating in grain growth or suppression of oxide material systems, and the corresponding grain growth mechanisms are not clear. Ren *et al.* reported that faster grain growth occurs at the center regime during flashing sintering 3 mol.% yttria-stabilized zirconia. This mainly results from the massive oxygen vacancies induced by large electric current, which significantly lowers the migration energy of cations leading to grain growth. However, the reduction of grain size was also observed at the cathode, which may be related to the massive recrystallization of zirconia induced by oxygen vacancies condensing to form voids [54]. Yoshida *et al.* reported that the grain size can be effectively suppressed for pure and TiO_2-doped Al_2O_3 ceramics sintered in N_2+5 % H_2 compared to air atmosphere at the same temperature [55]. Notably, by studying the grain growth behavior of Nd_2O_3-doped $BaTiO_3$ ceramics at different vacancy concentrations, An *et al.* revealed that the effects of donor concentration and vacancy concentration on grain growth behavior are related to their effect on grain boundary structure [56]. In our present work, the extra grain boundary oxygen vacancies can significantly enhance the grain boundary diffusion, which can accelerate densification rate of Al_2O_3 nanocrystalline ceramics but cannot cause grain growth owing to the unactivated grain boundary migration at lower temperatures.

The results obtained in the present work demonstrate the beneficial effects of low P_{O2} atmospheres (vacuum, N_2, and Ar) on the production of dense Al_2O_3 nanocrystalline ceramics of finer grains. Low P_{O2} atmospheres can reduce the E_a of grain boundary diffusion, which enhances mass transport at low temperature, probably through the generation of extra diffusion mechanisms induced by reduced P_{O2}. According to the previous studies reported in literature [15,31], grain boundary diffusion is recognized as the main mechanism of densification in fine-grained Al_2O_3 ceramics during pressureless sintering, which involves the diffusion of both aluminum and oxygen along grain boundaries. The predominant mechanism of mass transport in the Al_2O_3 ceramics is attributed to oxygen diffusion due to its lower diffusion rate triggered by its larger ionic radius [24-26,57,58]. Therefore, the reduction in E_a of grain boundary diffusion should be mainly related to the oxygen diffusion. Normally, point-defect models based on Wagner oxidation theory have historically been applied to explain the Al_2O_3 grain boundary diffusion, and the oxygen diffusivity can be expressed in terms of oxygen vacancy diffusivity using relevant equations,

$$D_O^{GB} C_O^{GB} = D_{V_O^{\bullet\bullet}}^{GB} C_{V_O^{\bullet\bullet}}^{GB} \quad (5)$$

where $D_{V_O^{\bullet\bullet}}^{GB}$ is the oxygen vacancy grain boundary diffusivity, and $C_{V_O^{\bullet\bullet}}^{GB}$

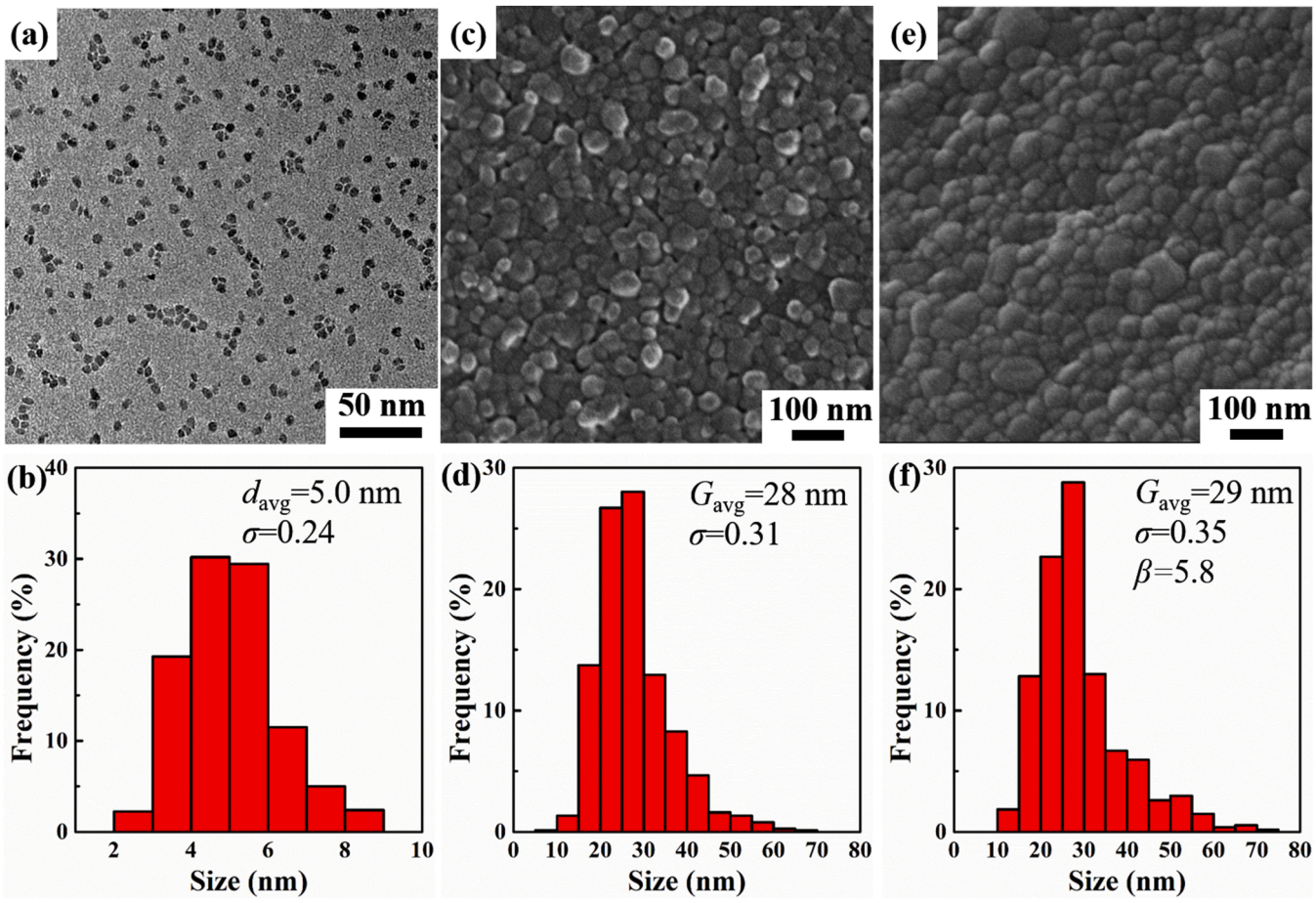

Fig. 8. TEM image (a) and particle size distribution (b) of α-Al_2O_3 nanoparticles. SEM images (c, e) and grain size distributions (d, f) of Al_2O_3 nanocrystalline ceramic sintered in N_2 at T_1 1000 ℃ without holding (c, d) and sintered in N_2 at T_1 1000 ℃ without holding and T_2 900 ℃ for 40 h (e, f).

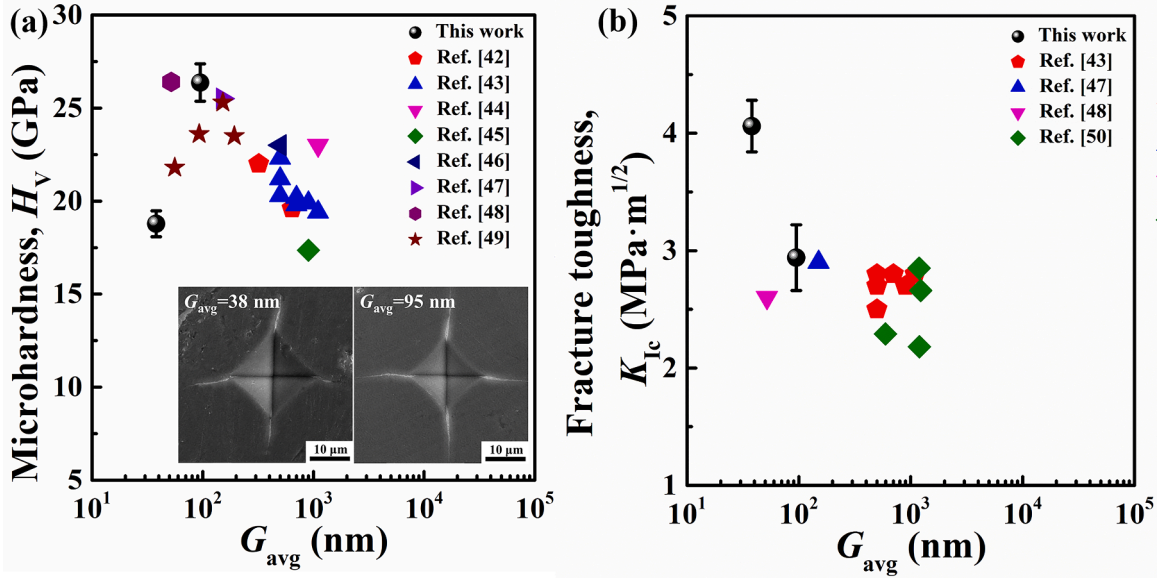

Fig. 9. Microhardness H_V (a) and fracture toughness K_{Ic} (b) as a function of average grain size G_{avg} for dense pure Al_2O_3 ceramics. The indentation images were inserted in the insets of (a).

presents the oxygen vacancy concentration in grain boundaries. $C_{V_O^{\bullet\bullet}}^{GB}$ is mainly dependent on the P_{O2} of sintering atmospheres and tends to decrease with increasing P_{O2} [28]. Generally, the relevant defect chemistry reaction within Al_2O_3 encompasses intricate reactions leading to the generation of defects, oxygen vacancies, and electron participate, which can be succinctly expressed as [25]

$$O_O^{\times} \xrightarrow{Al_2O_3} V_O^{\bullet\bullet} + 2e' + \frac{1}{2}O_2\uparrow \quad (6)$$

where $O_O^{\times}$ represents an oxygen anion, $V_O^{\bullet\bullet}$ is oxygen vacancy, and e' is electron. Further, the dependence of $C_{V_O^{\bullet\bullet}}^{GB}$ can be described by [25]

$$C_{V_O^{\bullet\bullet}}^{GB} \propto P_{O_2}^{-1/6} \quad (7)$$

It is widely recognized that subjecting Al_2O_3 to elevated temperatures in uniform environments leads to the formation of various defects such as Schottky pairs or Frenkel pairs [57]. Apart from these thermally generated defects, additional defects such as oxygen vacancies form when the material is placed in low P_{O2} atmospheres such as vacuum, N_2, and Ar. While the amount of reduction-generated oxygen vacancies in the bulk is expected to be small under weakly reducing atmospheres considering alumina's large bandgap, the amount of reduction-generated oxygen vacancies could be significant on the surfaces of Al_2O_3 nanoparticles and in the grain boundaries of Al_2O_3 nanocrystalline ceramics. This phenomenon can significantly accelerate oxygen diffusion along grain boundaries and promote densification of α-Al_2O_3 nanoparticles. In our present work, we found that fast densification of the α-Al_2O_3 nanoparticles occurs in vacuum, N_2, and Ar compared to air (Fig. 3a). In addition, the fastest densification can be achieved at lower temperatures for sintering in vacuum, N_2, and Ar than that in air (Fig. 3b). This fast densification at low sintering temperatures in vacuum, N_2, and Ar can be primarily attributed to the generation of extra oxygen vacancies in grain boundaries resulting from decreased P_{O2}. Notably, the formation of more oxygen vacancies induced by decreased P_{O2} in grain boundaries can result in a loose structure in grain boundaries, which can reduce the diffusion barrier resulting in the lower E_a for grain boundary diffusion and make the diffusion of atoms through grain boundaries easier at low temperatures [57]. As a result, the E_a values of the Al_2O_3 samples sintered in vacuum, N_2, and Ar are obviously smaller than those sintered in air, as shown in Fig. 5 and Table 2. Similarly, the lower E_a of oxygen grain boundary diffusion of non-doped polycrystal Al_2O_3 in low P_{O2} (10^{-8} and 10^{-4} Pa) conditions was also reported by Kitaoka *et al.* [57] and Matsudaira *et al.* [59] who evaluated the E_a values of oxygen grain boundary diffusion to be 395 and 506 kJ/mol, respectively, significantly lower than the values reported by Prot *et al.* (921 kJ/mol in undoped polycrystal Al_2O_3) [21] and Reddy (825 kJ/mol in polycrystal Al_2O_3) [60]. The reduction of E_a can be mainly attributed to the formation of extra oxygen vacancies, which preferentially exist in grain boundaries induced by low P_{O2} conditions. The formation of extra oxygen vacancies can reduce a barrier to grain boundary diffusion of oxygen, leading to the lower E_a [57,59].

Microhardness results of Al_2O_3 nanocrystalline ceramics exhibit apparent strengthening effect as the average grain size decreases to ~90 nm, probably attributed to the presence of massive grain boundaries in Al_2O_3 nanocrystalline ceramics inhibiting dislocation slip. Notably, Al_2O_3 nanocrystalline ceramics show obvious softening and toughening effects as the average grain size is reduced to 38 nm (Fig. 9). This phenomenon may be attributed to grain boundary softening instead of the dislocation slip mechanism. High volume fraction of grain boundaries may favor plastic deformation by grain boundary sliding and soften and toughen the material [61,62]. The decrease in H_V with reducing grain size was known as an inverse Hall Petch relationship, which was reported in several nanocrystalline ceramics (e.g., $MgAl_2O_4$ nanocrystalline ceramics and Al_2O_3/SiO_2 nanocrystalline composite ceramics) [62–64]. Our results demonstrate that the two-step sintered Al_2O_3 nanocrystalline ceramics with finer grain sizes (38 nm) and uniform microstructure (ultra-narrow grain size distribution with σ=0.34) show lower microhardness but higher fracture toughness. More detailed studies on the mechanical properties and plastic deformation mechanisms of Al_2O_3 nanocrystalline ceramics with different grain sizes will be reported in the future.

5. Conclusions

1. The feasibility of low P_{O2} atmospheres (vacuum, N_2, and Ar) for sintering dense Al_2O_3 nanocrystalline ceramics of finer grains by pressureless sintering was demonstrated. The results show that the vacuum, N_2, and Ar atmospheres can significantly promote the densification of α-Al_2O_3 nanoparticles without abnormal grain growth.
2. The kinetic results show that Al_2O_3 samples have lower activation energies for grain boundary diffusion in low P_{O2} atmospheres compared to air, which can be attributed to the formation of extra oxygen vacancies induced by decreased P_{O2}. The induced extra oxygen vacancies in grain boundaries can reduce the diffusion barrier and accelerate oxygen diffusion.
3. Dense fine-grained Al_2O_3 nanocrystalline ceramics can be prepared in vacuum, N_2, and Ar by two-step pressureless sintering. In particular, a fully dense Al_2O_3 nanocrystalline ceramic with a relative density of ρ=99.5 %, an average grain size of G_{avg}=29 nm, and a coarsening ratio of β=5.8 was sintered in N_2 using 5.0 nm α-Al_2O_3 nanoparticles and represents the finest grain size in dense Al_2O_3 nanocrystalline ceramics achieved so far by pressureless sintering.

CRediT authorship contribution statement

Yupeng Wang: Writing – review & editing, Writing – original draft, Formal analysis, Data curation, Conceptualization. **Hongbing Yang:** Formal analysis, Data curation. **Zhengjun Pei:** Data curation. **Bing Shen:** Data curation. **Jun Shao:** Data curation. **Masood Mukhtar:** Data curation. **Zhikun Ma:** Data curation. **Herbert Gleiter:** Supervision. **Yanhao Dong:** Writing – review & editing, Supervision, Conceptualization. **Tengfei Ma:** Writing – review & editing, Supervision, Conceptualization. **Jiangong Li:** Writing – review & editing, Supervision, Conceptualization.

Declaration of competing interest

The authors declare that they have no known competing financial interests or personal relationships that could have appeared to influence the work reported in this paper.

Acknowledgment

The authors from Lanzhou University acknowledge the support of the National Natural Science Foundation of China (No. 51772137).

References

[1] J. Karch, R. Birringer, H. Gleiter, Ceramics ductile at low temperature, Nature 330 (1987) 556–558.
[2] E.H. Penilla, L.F. Devia-Cruz, A.T. Wieg, P. Martinez-Torres, N. Cuando-Espitia, P. Sellappan, Y. Kodera, G. Aguilar, J.E. Garay, Ultrafast laser welding of ceramics, Science 365 (2019) 803–808.
[3] R.M. Laine, J.C. Marchal, H.P. Sun, X.Q. Pan, Nano-α-Al_2O_3 by liquid-feed flame spray pyrolysis, Nat. Mater. 5 (2006) 710–712.
[4] B. Conry, J.B. Harley, M.R. Tonks, M.S. Kesler, A.R. Krause, Engineering grain boundary anisotropy to elucidate grain growth behavior in alumina, J. Eur. Ceram. Soc. 42 (2022) 5864–5873.
[5] A.H. Heuer, M.Z. Azar, H. Guhl, M. Foulkes, B. Gleeson, T. Nakagawa, Y. Ikuhara, M.W. Finnis, The band structure of polycrystalline Al_2O_3 and its influence on transport phenomena, J. Am. Ceram. Soc. 99 (2016) 733–747.
[6] Y. Li, B. Shen, H. Yang, G. Hu, D. Yang, J. Wang, Y. Dong, J. Li, Alumina nanocrystalline ceramic by centrifugal casting, J. Eur. Ceram. Soc. 43 (2023) 1590–1596.
[7] N.M. Alford, J.D. Birchall, K. Kendall, Engineering ceramics–the process problem, Mater. Sci. Technol. 2 (1986) 329–336.
[8] Y. Dong, H. Yang, L. Zhang, X. Li, D. Ding, X. Wang, J. Li, J. Li, I.-W. Chen, Ultra-uniform nanocrystalline materials via two-step sintering, Adv. Funct. Mater. 31 (2021) 2007750.
[9] K. Bodišová, D. Galusek, P. Švančárek, V. Pouchlý, K. Maca, Grain growth suppression in alumina via doping and two-step sintering, Ceram. Int. 41 (2015) 11975–11983.

[10] J.M. McHale, A. Auroux, A.J. Perrotta, A. Navrotsky, Surface energies and thermodynamic phase stability in nanocrystalline aluminas, Science 277 (1997) 788–791.

[11] L. Li, S. Pu, Y. Liu, L. Zhao, J. Ma, J. Li, High-purity disperse α-Al_2O_3 nanoparticles synthesized by high-energy ball milling, Adv. Powder Technol. 29 (2018) 2194–2203.

[12] J. Li, S. Pu, W. Cao, L. Li, R. Guo, Comment on "high-surface-area corundum by mechanochemically induced phase transformation of boehmite, Science 368 (2020) eabb0142.

[13] I.-W. Chen, X.-H. Wang, Sintering dense nanocrystalline ceramics without final-stage grain growth, Nature 404 (2000) 168–171.

[14] X.-H. Wang, P.-L. Chen, I.-W. Chen, Two-step sintering of ceramics with constant grain-size, I. Y_2O_3, J. Am. Ceram. Soc. 89 (2006) 431–437.

[15] H. Yang, L. Li, W. Cao, Y. Liu, M. Mukhtar, L. Zhao, Y. Kang, Y. Dong, J. Li, Sintering kinetics and microstructure evolution in α-Al_2O_3 nanocrystalline ceramics: insensitive to Fe impurity, J. Eur. Ceram. Soc. 40 (2020) 1505–1512.

[16] M.N. Rahaman, Ceramic Processing and Sintering, Marcel Dekker, New York, 1995, p. 471.

[17] P.-L. Chen, I.-W. Chen, Sintering of fine oxide powders: I, microstructural evolution, J. Am. Ceram. Soc. 79 (1996) 3129–3141.

[18] P.-L. Chen, I.-W. Chen, Sintering of fine oxide powders: II, sintering mechanisms, J. Am. Ceram. Soc. 80 (1997) 637–645.

[19] Y. Lei, Y. Gong, Z. Duan, G. Wang, Density functional calculation of activation energies for lattice and grain boundary diffusion in alumina, Phys. Rev. B 87 (2013) 214105.

[20] P. Fielitz, K. Kelm, R. Bertram, A.H. Chokshi, G. Borchardt, Aluminium-26 grain boundary diffusion in pure and Y-doped polycrystalline α-alumina, Acta Mater. 127 (2017) 302–311.

[21] D. Prot, M.L. Gall, B. Lesage, A.M. Huntz, C. Monty, Self-diffusion in α-Al_2O_3 IV. oxygen grain-boundary self-diffusion in undoped and yttria-doped alumina polycrystals, Philos. Mag. A 73 (1996) 935–949.

[22] A.H. Heuer, T. Nakagawa, M.Z. Azar, D.B. Hovis, J.L. Smialek, B. Gleeson, N.D. M. Hine, H. Guhl, H.-S. Lee, P. Tangney, W.M.C. Foulkes, M.W. Finnis, On the growth of Al_2O_3 scales, Acta Mater. 61 (2013) 6670–6683.

[23] A.H. Heuer, Oxygen and aluminum diffusion in α-Al_2O_3: how much do we really understand? J. Eur. Ceram. Soc. 28 (2008) 1495–1507.

[24] R.L. Coble, Sintering alumina: effect of atmospheres, J. Am. Ceram. Soc. 3 (1962) 123–127.

[25] Y. Wang, H.M. Chan, J.M. Rickman, M.P. Harmer, Effect of oxygen partial pressure on grain-boundary transport in alumina, Acta Mater. 153 (2018) 205–213.

[26] T. Matsudaira, M. Wada, S. Kitaoka, Effect of dopants on the distribution of aluminum and oxygen fluxes in polycrystalline alumina under oxygen potential gradients at high temperatures, J. Am. Ceram. Soc. 96 (2013) 3243–3251.

[27] R.F. Walker, Mechanism of material transport during sintering, J. Am. Ceram. Soc. 38 (1955) 187–197.

[28] K. Kitazawa, R.L. Coble, Electrical conduction in single-crystal and polycrystalline Al_2O_3 at high temperatures, J. Am. Ceram. Soc. 57 (1974) 245–250.

[29] D. Han, J. Zhang, P. Liu, D. Wang, J. Wang, S. Wang, Effect of the pre-sintering atmosphere on the microstructures and optical qualities of transparent spinel ceramics, Ceram. Int. 48 (2022) 7806–7814.

[30] W. Cao, X. Mao, Y. Yuan, L. Li, L. Zhao, J. Li, Sintering kinetics of disperse ultrafine equiaxed α-Al_2O_3 nanoparticles, J. Eur. Ceram. Soc. 37 (2017) 4005–4013.

[31] H. Yang, L. Li, Y. Li, B. Shen, Y. Kang, L. Zhao, J. Li, Y. Dong, J. Li, Unveiling exceptional sinterability of ultrafine α-Al_2O_3 nanopowders, J. Materiom. 7 (2021) 837–844.

[32] G.B. Ghorbal, A. Tricoteaux, A. Thuault, G. Louis, D. Chicot, Comparison of conventional knoop and vickers hardness of ceramic materials, J. Eur. Ceram. Soc. 37 (2017) 2531–2535.

[33] G.R. Anstis, P. Chantikul, B.R. Lawn, D.B. Marshall, A critical evaluation of indentation techniques for measuring fracture toughness: I, direct crack measurements, J. Am. Ceram. Soc. 64 (1981) 533–538.

[34] L. Xu, Z. Xie, L. Gao, X. Wang, F. Lian, T. Liu, W. Li, Evaluation and characterization of alumina ceramics with elongated grains, Ceram. Int. 31 (2005) 953–958.

[35] D.E. Cox, A.R. Moodenbaugh, A.W. Sleight, H.-Y. Chen, Structural refinement of neutron and x-ray data by the rietveld method: application to Al_2O_3 and $BiVO_4$, NBS Spec. Publ. 567 (1980) 189–201.

[36] D.L. Johnson, New method of obtaining volume, grain-boundary, and surface diffusion coefficients from sintering data, J. Appl. Phys. 40 (1969) 192–200.

[37] S.-J.L. Kang, Y.-I. Jung, Sintering kinetics at final stage sintering: model calculation and map construction, Acta Mater. 52 (2004) 4573–4578.

[38] C. Herring, Effect of change of scale on sintering phenomena, J. Appl. Phys. 21 (1950) 301–303.

[39] J.D. Hansen, R.P. Rusin, M.-H. Teng, D.L. Johnson, Combined-stage sintering model, J. Am. Ceram. Soc. 75 (1992) 1129–1135.

[40] R. Guo, W. Cao, X. Mao, J. Li, Selective corrosion preparation and sintering of disperse α-Al_2O_3 nanoparticles, J. Am. Ceram. Soc. 99 (2016) 3556–3560.

[41] W. Cao, X. Mao, L. Li, B. Wang, Q. Guo, J. Li, Sintering of α-Al_2O_3 nanocrystalline ceramic from large α-Al_2O_3 polycrystalline nanoparticles, Ceram. Int. 43 (2017) 1378–1382.

[42] S. Ghanizadeha, S. Grasso, P. Ramanujam, B. Vaidhyanathan, J. Binner, P. Brown, J. Goldwasser, Improved transparency and hardness in α-alumina ceramics fabricated by high-pressure SPS of nanopowders, Ceram. Int. 43 (2017) 275–281.

[43] M.S. Boldin, A.A. Popov, A.V. Nokhrin, A.A. Murashov, S.V. Shotin, V. N. Chuvil'deev, N.Y. Tabachkova, K.E. Smetanin, Effect of grain boundary state and grain size on the microstructure and mechanical properties of alumina obtained by SPS: a case of the amorphous layer on particle surface, Ceram. Int. 48 (2022) 25723–25740.

[44] Z. Sun, B. Li, P. Hu, F. Ding, F. Yuan, Alumina ceramics with uniform grains prepared from Al_2O_3 nanospheres, J. Alloys Compd. 688 (2016) 933–938.

[45] S. Chang, R.H. Doremus, L.S. Schadler, R.W. Siegel, Hot-pressing of nano-size alumina powder and the resulting mechanical properties, Int. J. Appl. Ceram. Technol. 1 (2004) 172–179.

[46] W.-H. Chen, P.K. Nayak, H.-T. Lin, A.C. Lee, J.-L. Huang, Enhanced mechanical properties of WC-reinforced Al_2O_3 ceramics via spark plasma sintering, Ceram. Int. 41 (2015) 1317–1321.

[47] N. Nishiyama, T. Taniguchi, H. Ohfuji, K. Yoshida, F. Wakai, B.-N. Kim, H. Yoshida, Y. Higo, A. Holzheid, O. Beermann, T. Irifune, Y. Sakka, K.I. Funakoshi, Transparent nanocrystalline bulk alumina obtained at 7.7 GPa and 800℃, Scripta Mater. 69 (2013) 362–365.

[48] J. Zhang, F. Liu, P. Liu, D. He, Transparent alumina nanoceramics prepared under high pressure and low temperature, Adv. Eng. Mater. 25 (2023) 2101413.

[49] R.S. Mishra, C.E. Lesher, A.K. Mukherjee, High-pressure sintering of nanocrystalline γ-Al_2O_3, J. Am. Ceram. Soc. 79 (1996) 2989–2992.

[50] H. Belghalem, M. Hamidouche, L. Gremillard, G. Bonnefond, G. Fantozzi, Effect of spark plasma sintering of alumina nanopowder on the mechanical properties, J. Aust. Ceram. Soc. 53 (2017) 49–55.

[51] D. Liu, Y. Cao, J. Liu, Y. Gao, Y. Wang, Effect of oxygen partial pressure on temperature for onset of flash sintering 3YSZ, J. Eur. Ceram. Soc. 38 (2018) 817–820.

[52] H.-F. Ju, K. Ning, K. Lu, Atmosphere effects on micron-sized ZnO ridges during sintering, J. Eur. Ceram. Soc. 38 (2018) 5007–5014.

[53] V.V. Srdić, M. Winterer, H. Hahn, Sintering behavior of nanocrystalline zirconia prepared by chemical vapor synthesis, J. Am. Ceram. Soc. 83 (2000) 729–736.

[54] K. Ren, J. Xia, Y. Wang, Grain growth kinetics of 3 mol.% yttria-stabilized zirconia during flash sintering, J. Eur. Ceram. Soc. 39 (2019) 1366–1373.

[55] H. Yoshida, K. Hiraga, T. Yamamoto, Densification behavior of Ti-doped polycrystalline alumina in a nitrogen-hydrogen atmosphere, Mater. Trans. 5 (2009) 1032–1036.

[56] S.-M. An, S.-J.L. Kang, Boundary structural transition and grain growth behavior in $BaTiO_3$ with Nd_2O_3 doping and oxygen partial pressure change, Acta Mater. 59 (2011) 1964–1973.

[57] S. Kitaoka, T. Matsudaira, M. Wada, Mass-transfer mechanism of alumina ceramics under oxygen potential gradients at high temperatures, Mater. Trans. 50 (2009) 1023–1031.

[58] T. Matsudaira, M. Wada, T. Saitoh, S. Kitaoka, The effect of lutetium dopant on oxygen permeability of alumina polycrystals under oxygen potential gradients at ultra-high temperatures, Acta Mater. 58 (2010) 1544–1553.

[59] T. Matsudaira, M. Wada, T. Saitoh, S. Kitaoka, Oxygen permeability in cation-doped polycrystalline alumina under oxygen potential gradients at high temperatures, Acta Mater. 59 (2011) 5440–5450.

[60] K.P.R. Reddy, Oxygen Diffusion in Close Packed Oxides, Case Western Reserve Univ., Cleveland, OH, 1979. Ph.D. thesis.

[61] M.A. Meyers, A. Mishra, D.J. Benson, Mechanical properties of nanocrystalline materials, Prog. Mater. Sci. 51 (2006) 427–556.

[62] M. Sokol, M. Halabi, Y. Mordekovitz, S. Kalabukhov, S. Hayun, N. Frage, An inverse Hall-Petch relation in nanocrystalline $MgAl_2O_4$ spinel consolidated by high pressure spark plasma sintering (HPSPS), Scripta Mater. 139 (2017) 159–161.

[63] D. Ehre, R. Chaim, Abnormal Hall-Petch behavior in nanocrystalline MgO ceramic, J. Mater. Sci. 43 (2008) 6139–6143.

[64] N.A. Gaida, N. Nishiyama, A. Masuno, A. Holzheid, H. Ohfuji, U. Schürmann, C. Szillus, E. Kulik, J. Bednarcik, O. Beermann, C. Giehl, L. Kienle, Synthesis of Al_2O_3/SiO_2 nano-nano composite ceramics under high pressure and its inverse Hall-Petch behavior, J. Am. Ceram. Soc. 100 (2017) 323–332.